Unified Equivalent Steady-State Circuit Model and Comprehensive Design of the *LCC* Resonant Converter for HV Generation Architectures

Saijun Mao, *Member, IEEE*, Chengmin Li, Wuhua Li, *Member, IEEE*, Jelena Popović, *Member, IEEE*, Stefan Schröder, *Senior Member, IEEE*, and Jan Abraham Ferreira, *Fellow, IEEE*

***Abstract*—In this paper, a unified equivalent circuit model which can simplify the design and analysis of a family of high-voltage (HV) generation architectures based on the series–parallel (*LCC*) resonant converter is proposed. First, four HV generation architectures are reviewed in terms of the modularization level of HV transformers and rectifiers. Next, the steady-state, unified equivalent resistor and capacitor (*RC*) model that can be easily embedded into the resonant tank to replace the complex HV transformers and rectifiers is derived. The generic model can be applied to the HV generators with different architectures, different voltage multiplier topologies, stage, and polarities number. Further analysis of the power factor of the resonant tank, the voltage gain of HV generators, and electrical stresses of power components is achieved with the derived equivalent circuit model. The analysis reveals the inherent circuit properties among HV generators with different configurations. Subsequently, a comprehensive design methodology considering the power factor, conduction angle, and quality factor is presented, which leads to low electrical stresses on the components and high efficiency. Furthermore, the parameter selection constraint based on the power factor, conduction angle, and quality factor is derived, which can ensure the effective design outputs. Finally, the proposed unified equivalent model and comprehensive design methodology are validated by the experimental results of a 250 V input, 20 kV output 500 W HV generator hardware prototype with distributed transformers and voltage multipliers.**

***Index Terms*—Converter design, high-voltage (HV) generator, *LCC* resonant converter, steady-state model, voltage multiplier.**

NOMENCLATURE

M	Numbers of the transformer.
N	Stages of the voltage multiplier.
P	Polarities of the voltage multiplier.
K	Turns ratio of the high-voltage (HV) transformer.
I_{Lm}	Maximum resonant current.
$i_L(t)$	Instantaneous resonant current.
θ	Conduction angle.
f_s/ω_s	Frequency/angular frequency of the resonant tank input voltage.
v_p	Instantaneous voltage across the parallel capacitor.
i_s	Instantaneous current of the transformer secondary side.
$I_{s,\mathrm{avg}}$	Average current of the transformer secondary side.
$I_{s,\mathrm{RMS}}$	Root mean square (RMS) current of the transformer secondary side.
C_p	Parallel resonant capacitance.
V_o/I_o	Output voltage/current.
R_o/P_o	Output resistor/power.
k_{VM}	Voltage gain of the rectifier.
k_v	Coefficients of the Fourier transformation of the parallel capacitor voltage.
k_i	Coefficients of the Fourier transformation of the parallel capacitor current.
η	Efficiency of the HV generator.
R_{eq}	Equivalent resistance of the HV transformer loaded by the rectifier.
C_{eq}	Equivalent capacitance of the HV transformer loaded by the rectifier.
k_c	Coefficients between C_p and C_{eq}.
C_{tot}	Total capacitance of the equivalent *RC* network.
R_o'	Output resistor of the subdivided cell.
C_p'	Parallel capacitor of the subdivided cell.
R_{eq}'	Equivalent resistor of the subdivided cell.
C_{eq}'	Equivalent capacitor of the subdivided cell.
PF	Power factor of the resonant tank.
V_{in}	Input dc voltage.
$I_{\mathrm{in.RMS}}$	Input RMS current.
ψ	Phase lag between inverter output voltage and resonant current.
L_r	Resonant inductance.
L_{plk}	Primary side leakage inductance of the HV transformer.
L_{r_tot}	Total resonant inductance of the resonant tank.
C_r	Resonant capacitor.
Z_{in}	Resonant tank input impedance
V_{Cr}	Maximum voltage across the resonant capacitor.
$V_{cp,\max}$	Maximum voltage of the parallel capacitor.
Q	Quality factor of the resonant tank.
G_θ	Product of $\omega_s, C_{\mathrm{tot}}, R_{\mathrm{eq}}$.

Manuscript received May 10, 2017; revised September 6, 2017; accepted October 30, 2017. Date of publication November 14, 2017; date of current version June 22, 2018. Recommended for publication by Associate Editor J. Liu. *(Corresponding author: Saijun Mao.)*

S. Mao, J. Popović, and J. A. Ferreira are with Delft University of Technology, Delft 2628, The Netherlands (e-mail: maosaijun@126.com; J.Popovic@tudelft.nl; J.A.Ferreira@tudelft.nl).

C. Li and W. Li are with the College of Electrical Engineering, Zhejiang University, Hangzhou 310027, China (e-mail: lichengmin@zju.edu.cn; woohualee@zju.edu.cn).

S. Schröder is with GE Global Research, Munich 85748, Germany (e-mail: stefan.schroeder@research.ge.com).

Color versions of one or more of the figures in this paper are available online at http://ieeexplore.ieee.org.

Digital Object Identifier 10.1109/TPEL.2017.2774147

I. Introduction

HIGH-VOLTAGE (HV) generators are important building blocks of X-ray generators, electrostatic precipitators, plasma generators, etc. [1]–[4]. These HV generators convert low dc voltages to high dc voltages, typically in the range of tens to hundreds of kilovolts. The resonant-type power converters are the common topology choice in HV generator systems since they enable high power density, high efficiency, and fast dynamic performance.

Generally, an HV generator is composed of a high-frequency dc–ac inverter, a resonant tank, an HV transformer, and an HV rectifier, as illustrated in Fig. 1. Compared with other resonant-type converters, the series–parallel (*LCC*) resonant converter is more widely adopted in the HV generator due to its soft-switching capability, full parasitic component utilization of the HV transformer and its voltage boosting feature [5]. The HV generation circuit, as shown in Fig. 1, including the HV transformer and rectifier, is the crucial stage to achieve a large voltage gain.

Rectifiers have different configurations, such as the full-bridge rectifier, single or dual polarity half-wave Cockcroft–Walton (CW) voltage multiplier and full-wave CW voltage multiplier, as shown in Fig. 2. To achieve a HV gain, rated output power, as well as low-voltage stress on the power components, multiple transformers and multiple rectifiers can be utilized orderly to form different HV generation architectures. Four HV generator architectures are classified based on according to the level of modularity of the key power building blocks such as HV transformers and multiple rectifiers as shown in Fig. 3 [4].

The centralized architecture provides the advantages of the fast pulse speed and low-voltage ripple compared with the distributed architecture, but suffers from a larger insulation stress and less flexibility. In general, distributed architectures are preferred for a higher output voltage and power rating. An advantage of distributed architecture 4 is the modular structure, which enables the flexible combination of submodules to form higher power or higher output voltage. The diversity in HV generation architectures offers more alternatives in generating high output voltages. On the other hand, more challenges are added in modeling and analysis due to various topologies. A unified steady-state model is essential and helpful to investigate HV generator performance with the common architectures, which could offer effective guidelines in the HV generation topology selection and find general parameter design strategies.

Circuit modeling for the HV generator is challenging due to the complex operation modes and large values of transformer parasitics [26], [27]. The first harmonic approximation (FHA) is a classical modeling solution, which replace the voltages and currents by their fundamental components of the Fourier transformation to linearize the original circuit [28], [29]. In these linearized models [7], [8], [19], [22]–[25], [30], the behavior of the *LCC* converters with a simple full-bridge rectifier is described in detail.

Unfortunately, most state-of-the-art steady-state models are deduced only for the simple full-bridge rectifier and only for a specified architecture. The operation of the voltage multiplier fed by the *LCC* resonant tank is far more complex than that of the full-bridge rectifier. The state equation of a *LCC* converter feeding a three-stage full-wave CW voltage multiplier is proposed in [19], where the voltage multiplier is replaced by the one-stage CW rectifier and cannot represent the complex operation modes of the CW voltage multiplier. Generally, the modeling of the voltage multiplier fed by the *LCC* resonant tank and the various HV generation architectures are two remaining challenges to be solved. An FHA-based steady-state model is proposed in [31], where the HV transformer and the full-bridge rectifier are modeled by a resistor and capacitor (*RC*) network. This simple and extendable *RC* model is a promising solution to deduce a unified model of HV generation topologies. However, the model needs to be further improved to consider the various HV generator architectures with different voltage multiplier topologies, stage number, and polarities.

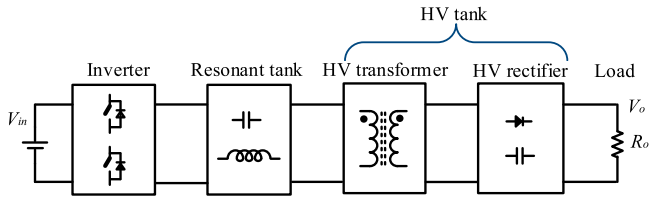

Fig. 1. Block diagram of HV generators.

In addition to the lack of unified circuit models, the design of the HV generator is also challenged by the high degree of design freedom. An iterative design procedure with the analytical *RC* model is given in [9]. A design based on the normalized characteristic diagram is given in [21]. In these design methods, some parameters are assumed to simplify the calculation. The parallel–series capacitor ratio $A = C_p/C_r$ is one of the most widely adopted assumption. However, the ratio *A* is not intuitive to reflect HV generator performance and does not ensure the overall optimized parameters. Moreover, the computer algorithms to search a large space of variables to acquire optimized designs are proposed in [10] and [18]. However, this approach is time consuming.

In this paper, a generic equivalent circuit model is proposed for various HV generator architectures with different voltage multiplier topologies, stage number, and polarities based on the FHA method. Further analysis on power factor, voltage gain, and electrical stresses of HV generators is investigated. Furthermore, the power factor, quality factor of the resonant tank, and conduction angle are utilized in the design process and a general constraint to select these parameters is proposed to ensure effective design outputs. Finally, comprehensive design is given and verified through a 250 V input, 20 kV output 500 W HV generator hardware prototype based on the HV generator architecture with distributed transformers and rectifiers.

The sections of this paper are organized as follows: Section II introduces the unified steady-state model of different HV generation architectures. Section III provides the analysis of power factor, voltage gain, electrical stresses of HV generators, and simulation verifications of the unified steady-state model. Section IV gives the comprehensive design of HV generator

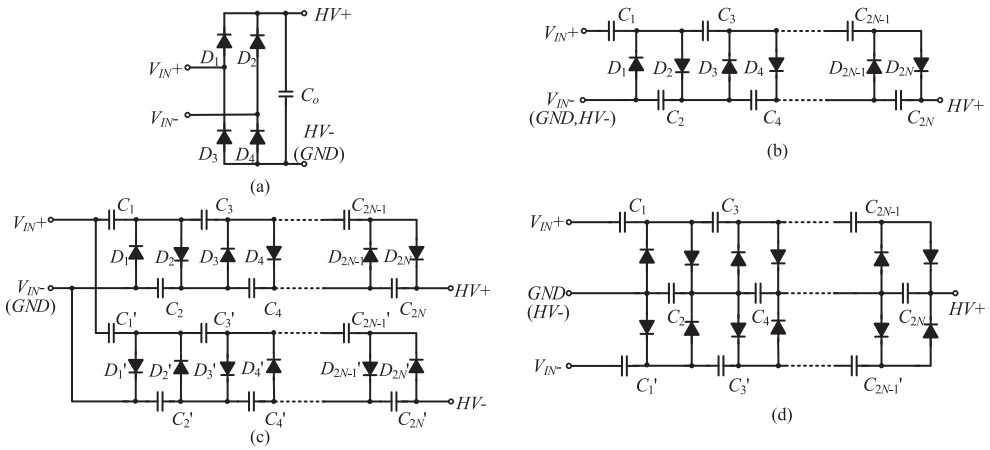

Fig. 2. Topologies of HV rectifiers. (a) Full-bridge rectifier [5]–[11]. (b) Single-polarity half-wave CW voltage multiplier [12]–[15]. (c) Dual polarity half-wave CW voltage multiplier [16], [17]. (d) Full-wave CW voltage multiplier [18], [19].

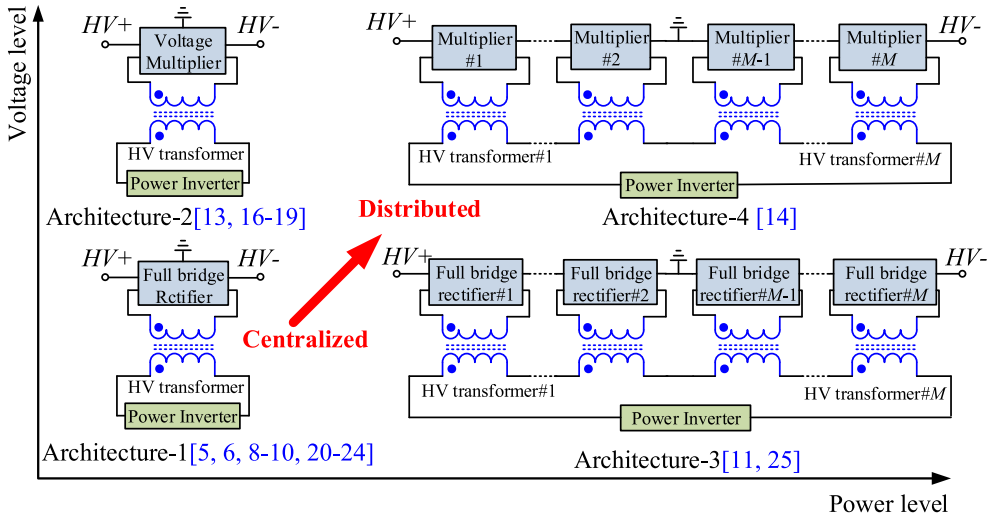

Fig. 3. Architectures of HV generators.

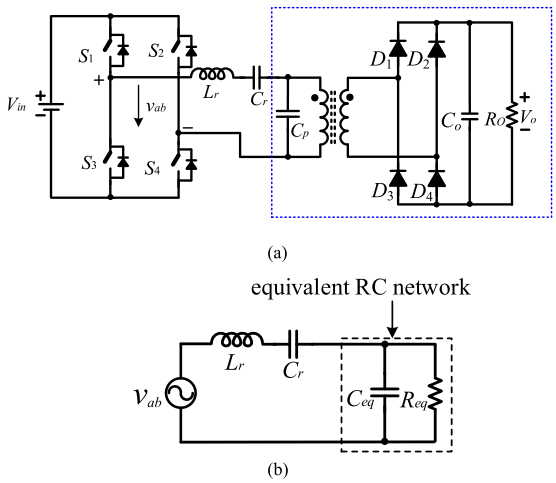

Fig. 4. *LCC* resonant converter with the full-bridge rectifier. (a) Circuit diagram of the *LCC* resonant converter with the full-bridge rectifier. (b) Equivalent circuit of the *LCC* resonant converter with the full-bridge rectifier proposed in [31].

based on power factor, quality factor, and conduction angle. Section V validates the proposed unified equivalent steady-state circuit model with the experimental testing results of the HV generator hardware prototype. Section VI concludes this paper.

II. Unified Steady-State Model of Different HV Generation Architectures

In this section, the analytical model of a voltage multiplier fed by the *LCC* resonant tank is derived first. Then, a unified model for the four architectures with different rectifiers topologies is given. To simplify the derivation of the steady-state model, the following assumptions are made.

1) The switching devices are ideal.
2) The quasi-sinusoidal resonant current $i_L(t)$ is equivalent to the ideal sinusoidal current, which is given by

$$i_L(t) = I_{Lm}\sin(\omega_s t). \tag{1}$$

3) The output voltage ripple and drop are ignored due to the large dc voltage and high operating frequency.

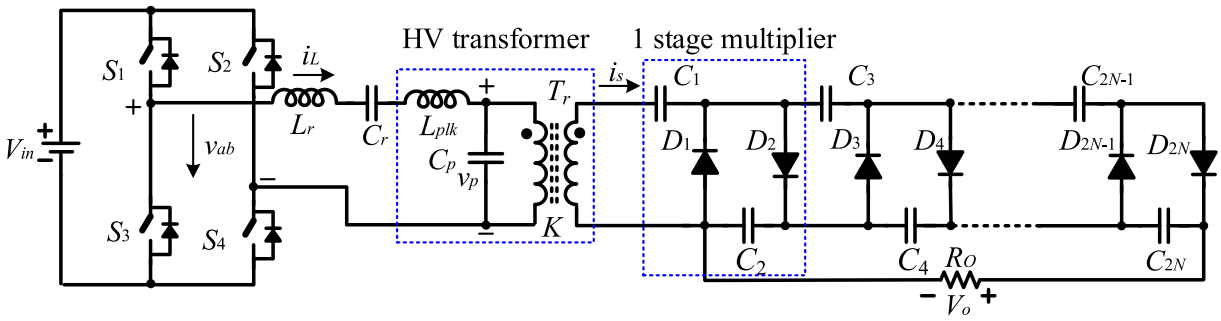

Fig. 5. Circuit diagram of the *LCC* resonant converter with the single-polarity voltage multiplier.

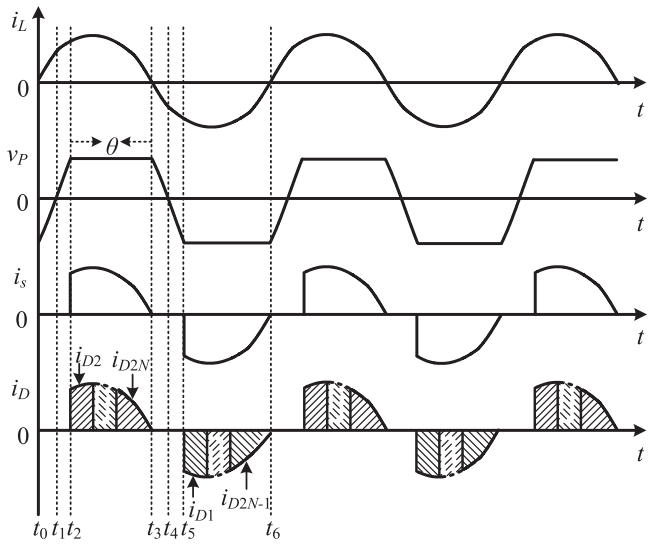

Fig. 6. Waveforms of the *LCC* resonant converter with the voltage multiplier.

A. Modeling of LCC Resonant Tank Fed by Half-Wave Single-Polarity Voltage Multiplier

Due to the high insulation requirements, the equivalent circuit model of the HV transformer is described by the series leakage inductance, the parallel winding capacitance reflected to the primary side and the ideal transformer [8]. Besides, the parasitic capacitance of rectifiers affects the operation of the *LCC* resonant converter [33] and needs to be considered.

The widely used analytical model of the *LCC* resonant converter is proposed in [31], where the HV transformer with a full-bridge rectifier is replaced by an equivalent *RC* network, as shown in Fig. 4. However, for the *LCC* resonant converter with single-polarity voltage multiplier shown in Fig. 5, the output capacitors are charged in parallel and discharged in series. The voltage gain and current distribution among the output diodes should be considered as opposed to the case of the full-bridge rectifier. Thus, an improved *RC* model needs to be derived.

The typical waveforms of *LCC* resonant converter with voltage multiplier is given in Fig. 6. By replacing v_P and i_s with fundamental element of the Fourier transformation, the equivalent resistance $R_{\rm eq}$ and capacitance $C_{\rm eq}$ is calculated by the impedance of the transformer input side. The derivation methodology is similar to [31] and takes the voltage gain and current gain of voltage multiplier into consideration. Hence, the detailed calculation is skipped for brevity. The derived $R_{\rm eq}$ and $C_{\rm eq}$ are given by

$$R_{\rm eq} = \frac{\eta {k_v}^2 R_o}{2K^2 {k_{\rm VM}}^2}$$
$$C_{\rm eq} = k_c C_p \tag{2}$$

where η is the conversion efficiency of the HV generation circuit, K is the turns ratio of the HV transformer, and $k_{\rm VM}$ is the voltage gain of the voltage multiplier, which is

$$k_{\rm VM} = \frac{V_o}{V_{\rm sec}} = 2N. \tag{3}$$

The coefficients k_v and k_c originate from the Fourier analysis of the waveforms and are given by

$$a_{v1} = \frac{2}{\pi}\left(\frac{\sin(\theta) - \pi + \theta}{1+\cos(\theta)} - \sin(\theta)\right)$$
$$b_{v1} = \frac{2}{\pi}(1-\cos(\theta))$$
$$k_v = \sqrt{a_{v1}^2 + b_{v1}^2}$$
$$k_c = \frac{2}{k_v(1+\cos(\theta))}\left(\frac{-a_{v1}}{k_v} - \frac{1}{\pi}\sqrt{\left(\frac{1}{2} - \frac{\cos(2\theta)}{2}\right)^2 + \left(\pi - \theta + \frac{\sin(2\theta)}{2}\right)^2}\right). \tag{4}$$

The conduction angle θ is the interval when the voltage of the HV transformer is clamped by the output capacitors. It is calculated by

$$\theta = 2\arctan\sqrt{\frac{{k_{\rm VM}}^2 K^2 \pi}{2\omega_s C_p R_o}}. \tag{5}$$

The total parallel capacitance of the HV generation circuit is

$$C_{\rm tot} = C_P + C_{\rm eq} = (1+k_c)\, C_P. \tag{6}$$

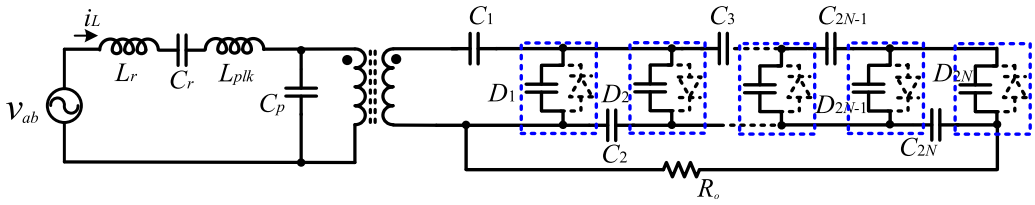

Fig. 7. Equivalent circuit model during the nonconductive interval $[t_0, t_2]$ and $[t_3, t_5]$ of multiplier diodes.

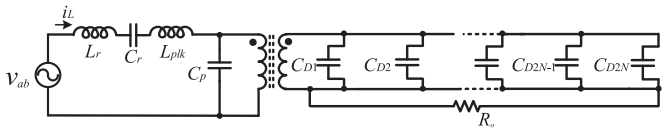

Fig. 8. Simplified equivalent circuit model during the nonconductive interval $[t_0, t_2]$ and $[t_3, t_5]$ of multiplier diodes.

The expression of $R_{\rm eq}, C_{\rm eq}$ is also applicable for the full-bridge rectifier or the full-wave CW voltage multiplier. The detailed derivation procedure is similar and skipped in this paper. $k_{\rm VM} = 1$ is established for the full-bridge rectifier.

During the nonconductive interval $[t_0, t_2]$ and $[t_3, t_5]$ of the multiplier diodes, as shown in Fig. 6, the parasitic capacitors of the diodes are charged by the output current of the HV transformer. The equivalent circuit model during the nonconductive interval $[t_0, t_2]$ and $[t_3, t_5]$ of the voltage multiplier diodes is illustrated in Fig. 7. In this period, the charge current loop contains the voltage multiplier capacitors and the parasitic capacitors, since the output capacitors are far larger than the parasitic capacitors, the voltage drop across the output capacitors caused by the charge current can be ignored and all output capacitors can be viewed as shorted together approximately, as shown in Fig. 8. As a result, all parasitic capacitors of the diodes are connected in parallel and can be included into the parallel capacitance C_p.

B. Generic Model of Four HV Generator Architectures

Considering the four HV generator architectures in Fig. 3, an HV transformer loaded by the full-bridge rectifier or the voltage multiplier is the basic structure of the HV generation circuits. As the basic structure has been modeled by an equivalent *RC* model, the model of the combined architectures is established by decomposing architectures into the basic structure. Since architecture 4 is the most complex architecture, modeling of architecture 4 is presented in detail.

Fig. 9 demonstrates the subdivision process of architecture 4 with M distributed transformers loaded by N-stage half-wave voltage multipliers. As shown in Fig. 9(a), due to symmetry, the output voltage of each voltage multiplier is equal. Hence, architecture 4 can be equally divided into *M* parts separately, without making difference on the input side. Besides, for the dual polarity $(P = 2)$ CW voltage multiplier, the positive half-output voltage/current symmetrically equals to the negative half-output voltage and current. Each multiplier is further divided into P single-polarity N-stage voltage multipliers connected in parallel which makes no difference on the input side of the voltage multiplier. As a result, architecture 4 is split into $M \times P$ basic structures separately, as illustrated in Fig. 9(b). Each part is modeled individually by an equivalent parallel resistor and capacitor, as shown in Fig. 9(c). Finally, a merged equivalent *RC* model is acquired in Fig. 9(d).

In the subdivided single-polarity half-wave CW voltage multiplier, the output resistor is

$$R_o' = \frac{R_o}{M \cdot P}. \tag{7}$$

The parallel capacitor is

$$C_P' = \frac{C_P}{P}. \tag{8}$$

The conduction angle, equivalent resistor, and capacitor of the split HV transformer loaded by the CW voltage multiplier are calculated by replacing the output resistor and parallel capacitor in (5) and (2) with (7) and (8). The total equivalent capacitance and resistance of the HV tank are calculated by

$$\begin{aligned} R_{\rm eq} &= \frac{M}{P} R_{\rm eq}' \\ C_{\rm eq} &= \frac{P}{M} C_{\rm eq}'. \end{aligned} \tag{9}$$

Since there are M parallel capacitors connected in series, the total input parallel capacitance of the HV generation circuit is

$$C_{\rm tot} = \frac{C_P}{M} + C_{\rm eq} = \left(\frac{1}{M} + k_c\right) C_P. \tag{10}$$

The M leakage inductors of HV transformers are connected in series; thus, the total resonant inductance of the *LCC* resonant tank is

$$L_{r\_\rm tot} = L_r + M L_{\rm plk}. \tag{11}$$

It is evident that the modeling procedure of architecture 4 can be applied to the other distributed architectures by assigning numbers of transformers (M), stages of voltage multipliers (N), and polarities (P) of the voltage multiplier accordingly, as shown in Table I.

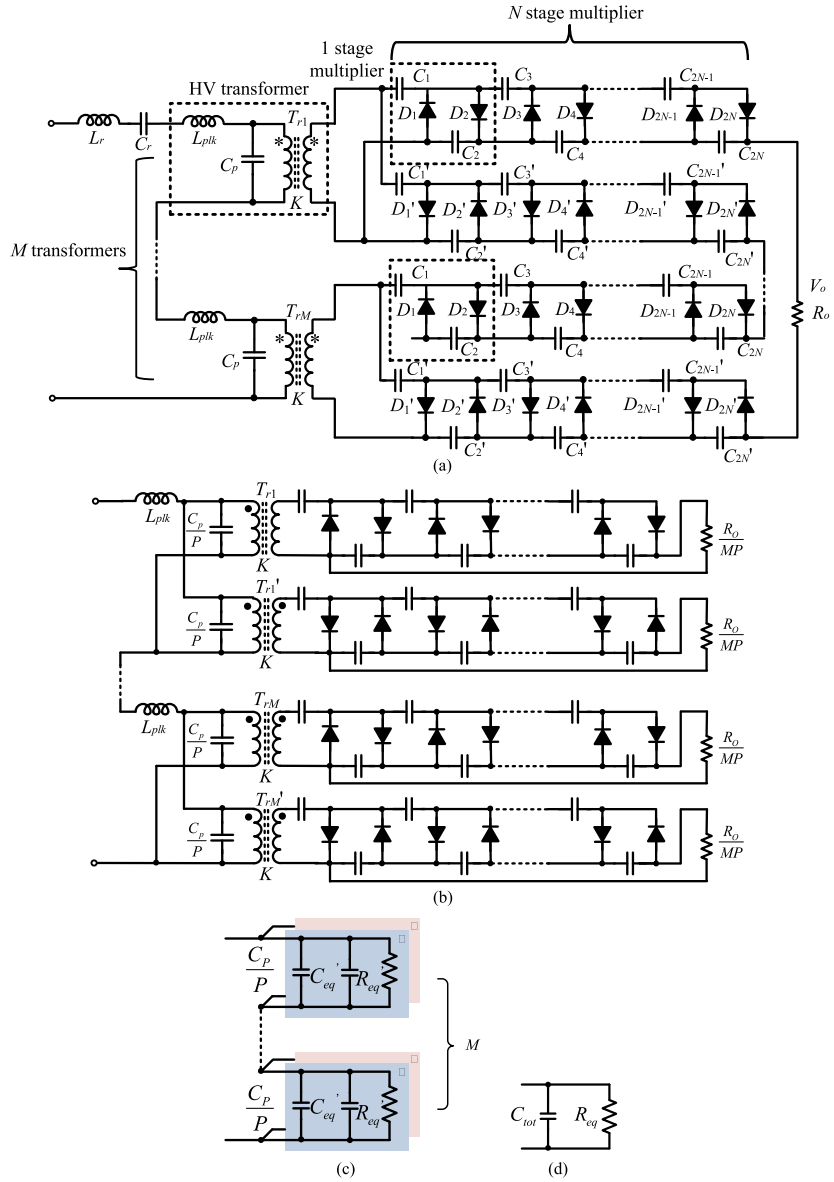

Fig. 9. Modeling of HV generator architecture 4. (a) Topology of architecture 4. (b) Input-side equivalent transformation. (c) Equivalent *RC* network (d) Merged equivalent *RC* model.

Above all, a general model of the four architectures is concluded by

$$k_{\mathrm{VM}} = \begin{cases} 2N, \text{voltage multiplier} \\ 1, \text{diode rectifier} \end{cases}$$

$$\theta = 2\arctan\sqrt{\frac{MP^2{k_{\mathrm{VM}}}^2K^2}{4f_sC_PR_o}}$$

$$R_{eq} = \frac{\eta k_V^2}{2P^2K^2k_{\mathrm{VM}}^2}\cdot R_o$$

$$C_{\mathrm{tot}} = \frac{(1+k_c)\,C_P}{M} \tag{12}$$

where k_v and k_c are calculated in (4). By replacing the highly nonlinearity HV generation circuit with the equivalent *RC* model, the analysis of the HV generator is significantly simplified.

III. HV Generators Analysis and Simulation Verifications of the Unified Steady-State Model

Based on the equivalent *RC* model, further analysis including the power factor of the resonant tank, voltage gain, quality factor, and stresses of devices is given in this section. These are important parameters to analyze the performance and facilitate the design of the HV generators.

A. Power Factor

The power factor of the resonant tank is defined as the ratio of real power flowing to the resonant tank and the apparent power which is the product of RMS value of input voltage and current.

TABLE I
PARAMETERS TO DESCRIBE THE FOUR ARCHITECTURES

Architecture	Numbers of transformers	Stages of voltage multipliers	Polarity
1	1	1	1
2	1	*N*	*P*
3	*M*	1	1
4	*M*	*N*	*P*

This yields

$$PF = \frac{P_o}{\eta V_{\text{in}} I_{\text{in,RMS}}} \tag{13}$$

where P_{o} is the output power, V_{in} is the input voltage, and $I_{\text{in,RMS}}$ is the RMS value of the input current. ψ is defined as the phase angle between the fundamental components of resonant tank input voltage and resonant current. Since the energy is only transferred by the fundamental components, PF is expressed by [11]

$$PF = \frac{2\sqrt{2}}{\pi}\cos\psi. \tag{14}$$

The equivalent circuit of the resonant tank in steady state is depicted in Fig. 4. The impedance of the resonant tank is

$$Z_{\text{in}} = j\omega_s L_{r\_\text{tot}} + \frac{1}{j\omega_s C_r} + \frac{R_{\text{eq}}}{1 + j\omega_s C_{\text{tot}} R_{\text{eq}}} = |Z_{\text{in}}|\angle\psi. \tag{15}$$

Solving (15), the power factor angle is calculated by

$$\psi = \arctan\left(\frac{1}{\left(\frac{\omega_s L_{r\_\text{tot}}}{R_{\text{eq}}} - \frac{1}{\omega_s C_r R_{\text{eq}}}\right)\left(1 + (\omega_s C_{\text{tot}} R_{\text{eq}})^2\right) - \omega_s C_{\text{tot}} R_{\text{eq}}}\right). \tag{16}$$

B. Voltage Gain

Ignoring the output voltage ripple, the output power is

$$P_o = V_o I_o. \tag{17}$$

Substituting (13) and (14) into (17) yields

$$\frac{V_o}{V_{\text{in}}} = \frac{2\sqrt{2}\eta\cos(\psi)}{\pi}\cdot\frac{I_{\text{in,RMS}}}{I_o} = \frac{2\sqrt{2}\cos(\psi)}{\pi}\cdot\frac{I_{\text{in,RMS}}}{I_{Lm}} \cdot\frac{I_{Lm}}{I_{s,\text{avg}}}\cdot\frac{I_{s,\text{avg}}}{I_o}. \tag{18}$$

For the full-bridge inverter, the input current is

$$i_{\text{in}}(t) = \begin{cases} I_{Lm}\sin(\omega_s t), -\psi \le \omega_s t \le \pi - \psi \\ -I_{Lm}\sin(\omega_s t), \pi - \psi \le \omega_s t \le 2\pi - \psi. \end{cases} \tag{19}$$

The RMS value of the input current is calculated by

$$I_{in,\text{RMS}} = \frac{I_{Lm}}{\sqrt{2}}. \tag{20}$$

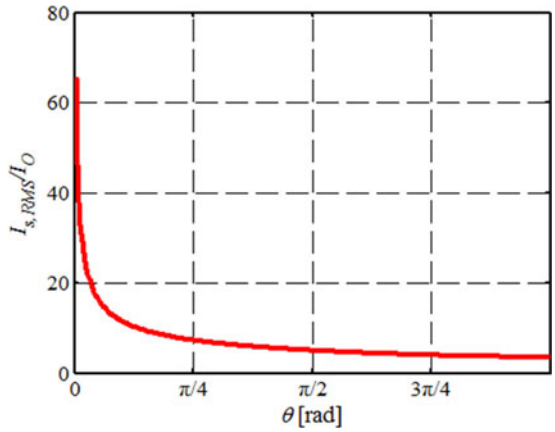

Fig. 10. RMS value of secondary-side current versus conduction angle $(N = 2, P = 2, \eta = 1)$.

From Fig. 6, the coefficients between the resonant current I_{Lm} and transformer secondary side average current $I_{s,\text{avg}}$ is

$$\frac{I_{Lm}}{I_{s,\text{avg}}} = \frac{K\pi}{2\sin^2\left(\frac{\theta}{2}\right)}. \tag{21}$$

Substituting (3), (20), and (21) into (18) yields

$$\frac{V_o}{V_{\text{in}}} = \frac{\eta P K k_{\text{VM}}\cos\psi}{\sin^2\left(\frac{\theta}{2}\right)}. \tag{22}$$

Equation (22) demonstrates that the stages and polarities of the voltage multiplier, turns ratio of the HV transformer, power factor, and conduction angle contribute to the HV gain. For the *LCC* resonant converter, the conduction angle is due to the parallel capacitor. $\theta \subset (0, \pi)$ yields

$$\frac{1}{\sin^2\left(\frac{\theta}{2}\right)} \ge 1. \tag{23}$$

It is indicated that the *LCC* resonant converter is especially suitable for the HV generation applications since the conduction angle contributes to the voltage gain. When the conduction angle decreases, the voltage gain increases. For the same voltage gain, the turns ratio of the HV transformer or the stages of the voltage multiplier is reduced.

C. Electrical Stresses

To compare different designs, the electrical stresses on the components are derived under the condition that the input voltage, output voltage, and output power are defined. From (13), the resonant current is

$$I_{Lm} = \frac{\pi}{2\eta\cos\psi}\cdot\frac{P_o}{V_{\text{in}}}. \tag{24}$$

The voltage of the resonant capacitor is

$$V_{Cr} = \frac{\pi}{2\eta\cos\psi}\cdot\frac{P_o}{\omega_s C_r V_{\text{in}}}. \tag{25}$$

Equations (24) and (25) indicate that the resonant current and series capacitor voltage are inversely proportional to the power

TABLE II
PARAMETERS OF THE HV GENERATORS

	No.	V_o/kV	P_o/kW	L_r/μH	C_r/nF	C_p/nF	K	M	N	P
Architecture 1	(1)	20.00	0.50	138.8	2.2	1.5	44.4	1	1	1
	(2)	20.00	20.00	34.7	6.6	4.6	66.7	1	1	1
	(3)	100.00	0.50	138.8	12.3	1.2	111.1	1	1	1
	(4)	100.00	20.00	34.7	49.1	4.6	111.1	1	1	1
Architecture 2	(5)	20.00	0.50	138.8	1.6	1.2	5.6	1	3	2
	(6)	20.00	20.00	37.9	6.3	5.0	4.6	1	3	2
	(7)	100.00	0.50	101.5	4.6	1.5	13.9	1	4	2
	(8)	100.00	20.00	34.7	6.6	4.6	20.8	1	4	2
Architecture 3	(9)	20.00	0.50	89.7	4.1	5.1	57.1	2	1	1
	(10)	20.00	20.00	22.4	13.0	18.5	74.8	2	1	1
	(11)	100.00	0.50	138.8	2.2	6.2	222.2	4	1	1
	(12)	100.00	20.00	24.1	11.4	23.4	375.0	4	1	1
Architecture 4	(13)	20.00	0.50	138.8	2.2	3.1	5.6	2	2	2
	(14)	20.00	20.00	34.7	6.6	9.3	8.3	2	2	2
	(15)	100.00	0.50	138.8	12.3	2.3	9.3	2	3	2
	(16)	100.00	20.00	34.7	6.6	9.3	27.8	2	3	2

TABLE III
COMPARISON BETWEEN THE SIMULATION (SIM.) AND MODEL

No.	V_o/kV			I_{Lm}/A			I_s/A		
	Sim.	Model	Error	Sim.	Model	Error	Sim.	Model	Error
(1)	19.62	20.00	1.9%	3.35	3.5	4.2%	0.0037	0.0039	5.4%
(2)	19.45	20.00	2.8%	13.31	14.0	4.9%	0.1258	0.1328	5.6%
(3)	98.20	100.00	1.8%	3.28	3.5	6.4%	0.0094	0.0098	4.0%
(4)	98.18	100.00	1.9%	13.59	14.0	2.7%	0.0039	0.0039	0.0%
(5)	20.49	20.00	–2.4%	3.58	3.5	–2.5%	0.3934	0.3985	1.3%
(6)	23.50	20.00	–14.9%	17.43	13.2	–24.1%	1.8252	1.6959	–7.1%
(7)	96.23	100.00	3.9%	3.16	3.5	6.1%	0.1167	0.1257	7.7%
(8)	99.20	100.00	0.8%	13.76	14.0	1.5%	0.4112	0.4251	3.4%
(9)	19.12	20.00	4.6%	4.46	4.5	0.7%	0.0039	0.0039	0.0%
(10)	19.54	20.00	2.4%	18.16	18.0	–1.1%	0.1420	0.1413	–0.5%
(11)	95.02	100.00	5.2%	3.50	3.5	–0.3%	0.0077	0.0079	2.0%
(12)	93.34	100.00	3.8%	15.15	15.7	3.7%	0.0253	0.0266	4.9%
(13)	20.38	20.00	–1.9%	3.55	3.5	–1.7%	0.3030	0.3142	3.7%
(14)	22.00	20.00	–9.1%	12.75	14.0	9.8%	1.1097	1.0627	–4.2%
(15)	95.67	100.00	4.5%	2.37	3.5	4.2%	0.1128	0.1179	4.5%
(16)	98.17	100.00	1.9%	13.70	14.0	2.4%	0.3065	0.3188	4.0%

factor. To reduce the voltage and current stresses, the power factor should be selected as large as possible.

The voltage stress of the parallel capacitor is

$$V_{Cp,\max} = \frac{\pi(1+cos\theta)}{4\eta\cos\psi\cdot\omega_s C_P}\cdot\frac{P_o}{V_{\rm in}}. \tag{26}$$

From Fig. 6, the RMS value of the transformer secondary side current is given by

$$I_{s,\rm RMS} = \frac{I_{Lm}}{K}\sqrt{\frac{2\theta-\sin 2\theta}{4\pi}}. \tag{27}$$

To analyze the influence of the conduction angle on the RMS value of the transformer secondary side current, utilizing (22) and (27) to eliminate K gives

$$\frac{I_{s,\rm RMS}}{I_o} = \frac{\eta NP\sqrt{\pi(2\theta-\sin 2\theta)}}{4\sin^2\left(\frac{\theta}{2}\right)}. \tag{28}$$

Fig. 10 displays the example of the relationship between the RMS value of the secondary side current and conduction angle. In the low conduction angle region, $I_{s,\rm RMS}$ increases dramatically. Hence, low θ is not recommended to reduce the power losses of the HV transformer secondary side.

D. Simulation Verification of the Proposed Model and Analysis

To verify the presented model, HV generators with the four architectures are simulated and compared with the proposed model. The parameters of the HV generators are designed to meet the output voltage V_o and output power P_o specifications, as shown in Table II. The switching frequency is chosen to be at 400 kHz and the input voltage is 250 VDC. The comparison between the proposed model and the simulation are given in Table III. In most cases, the error is below 6%, which verifies the validity of the proposed model. However, the large error occurs at design (6) and (14), where the dual polarity four-stage

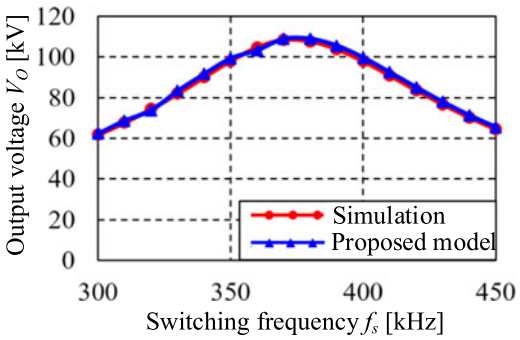

Fig. 11. Frequency response of the output voltage by simulation and proposed model.

voltage multipliers are adopted and the output current is relatively large. In large output current cases, the voltage ripple and drop of the voltage multiplier cannot be ignored and the modeling assumption 3 is not satisfied. As a result, a large deviation occurs in the Fourier analysis. This leads to a large modeling error. So, the proposed model is only suitable for low output voltage ripple conditions.

In the resonant type HV generators, the output voltage changes with the switching frequency. The frequency response of design (16), with multiple HV transformers and dual polarity rectifiers, is simulated and calculated as an example. As displayed in Fig. 11, the simulation shows a perfect alignment with the mathematical model, which verifies validity of the proposed model in the given frequency range.

IV. Comparison Comprehensive Design Procedure of the HV Generator Based on Power Factor, Quality Factor, and Conduction Angle

A comprehensive HV generator design method is proposed in this section to achieve the required voltage gain at the optimal efficiency, high power density, and low-voltage and current stress of the components. The design discussed here mainly focuses on the resonant tank and the HV transformer, while components such as the output capacitor and the switching devices are not discussed.

The power factor, conduction angle, and quality factor are selected to support the design of the HV generator. In the proposed analytical model, the power factor angle and the conduction angle are two characteristic parameters describing the properties of the HV generator. The voltage gain and the component stresses can be calculated directly from these parameters. This is different to the widely adopted design assumption $A = C_p/C_r$ is not practical to reflect the performance of the HV generator. In addition, a high-quality factor of the resonant tank is preferred to produce high fidelity sinusoidal current to reduce the component stress.

Moreover, previous modeling and design approaches usually neglect the power loss of the HV generator. The power losses of the HV high-frequency transformer and rectifier are relatively large, which introduces a large error in the mathematical model. It is very complex to model the power loss of the HV generator and rectifier. Based on test results of previous prototypes, the efficiency of the HV generation circuit at rated output is usually around $\eta = 0.80$. This value could be adopted in the design instead of the complex loss analysis.

In the design, the following specifications are given as inputs.

1) Input voltage $V_{\rm in}$, output voltage V_O, and output current I_O.
2) The chosen architecture. Fig. 3 offers some advices on the selection of architecture. Then, the number of transformers M and the polarity of voltage multiplier P is determined previously.
3) The HV transformer output voltage $V_{\rm sec}$. Unlike the case of the low-voltage transformers, the output voltage of the HV transformer is limited by HV insulation materials and packaging, thus needs to be determined with priority over the other parameters.

Then parameters of the HV generator are calculated step by step. The voltage multiplier stage number N is calculated by

$$N = \frac{1}{2P} \cdot \frac{V_o}{V_{\rm sec}}. \tag{29}$$

From (22), the turns ratio of the HV transformer is

$$K = \frac{\sin^2\left(\frac{\theta}{2}\right)}{2\eta NP\cos\psi} \cdot \frac{V_o}{V_{\rm in}}. \tag{30}$$

The selection of the values for the conduction angle θ and power factor angle ψ will be discussed later. From (12), the parallel capacitor is calculated by

$$C_P = \frac{MNP^2 k_{\rm VM} k^2}{2f_s R_o \tan^2\left(\frac{\theta}{2}\right)}. \tag{31}$$

The equivalent resistor and capacitor values are calculated from (12).

The quality factor of the resonant tank is defined as the ratio between stored energy and dissipated energy in the circuit. For the circuit shown in Fig. 4, the quality factor Q is calculated by

$$Q = \frac{1 + (\omega_s C_{\rm tot} R_{\rm eq})^2}{R_{\rm eq}} \cdot \sqrt{\frac{(L_r + ML_{\rm plk})}{C_r} + \frac{(L_r + ML_{\rm plk})(\omega_s C_{\rm tot} R_{\rm eq})^2}{C_{\rm tot}\left(1 + (\omega_s C_{\rm tot} R_{\rm eq})^2\right)}}. \tag{32}$$

From (12), the product $\omega_s C_{\rm tot} R_{\rm eq}$ is expressed by

$$G_\theta = \omega_s C_{\rm tot} R_{\rm eq} = \frac{\pi(1 + k_c)k_v^2}{4\eta \tan^2\left(\frac{\theta}{2}\right)}. \tag{33}$$

Equation (33) demonstrates that G_θ is only a function of the conduction angle. To simplify the calculation of G_θ, the right side of (34) can be approximated by

$$G_\theta \approx \frac{1}{\eta}\cot^2\left(\frac{\theta}{2}\right). \tag{34}$$

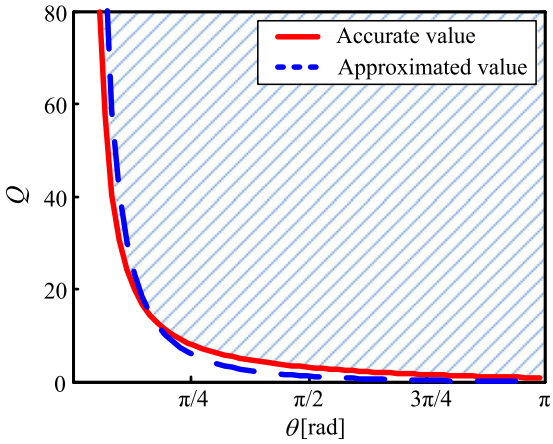

Fig. 12. Q–θ curve at $\cos\psi = 0.88$.

From (16) and (32), L_r and C_r are given by

$$L_{r\_\mathrm{tot}} = \frac{\tan\psi + \sqrt{\tan\psi^2 + 4Q^2}}{2\left(1 + {G_\theta}^2\right)} \cdot \frac{R_{\mathrm{eq}}}{\omega_s}$$

$$C_r = C_{\mathrm{tot}} \cdot \frac{1}{\frac{2Q^2}{G_\theta\left(\tan\psi + \sqrt{\tan\psi^2 + 4Q^2}\right)} - 1} \cdot \left(1 + \frac{1}{{G_\theta}^2}\right). \tag{35}$$

As given in (35), to ensure C_r is larger than zero, the following inequality must be satisfied:

$$Q > \sqrt{G_\theta^2 + G_\theta} \cdot \tan\psi. \tag{36}$$

Equation (36) demonstrates that there is a general constraint independent of the architecture. Fig. 12 demonstrates the boundary of (36) at $cos\psi = 0.88$. The solid curve is plotted using the exact value of G_θ, while the dashed curve is plotted using the approximated value of G_θ. The Q and θ value should be selected in the shaded region to give desired design outputs.

Generally, PF, Q, and θ are determined based on the following considerations.

1) Power factor: small power factor means large circulating energy between the resonant tank and the dc source. As a result, the device current stresses and resonant tank conduction losses will increase. The PF is desired to be as large as possible. However, if the power factor angle is near zero, which means that the instant current at commutation time of the inverter is near zero, there is not enough energy to ensure soft switching of switches. Hence, there exists a tradeoff in selecting a proper power factor for the resonant tank in the design. The $PF = 0.88$ is suggested to achieve the low circulating energy and zero-voltage switching of the inverter.
2) Conduction angle θ: from the voltage gain perspective, the conduction angle should be selected as small as possible to reduce the turns ratio of the HV transformer and the stages of the voltage multiplier. However, the voltage stress of the parallel capacitor and the current of the transformer secondary side are increased as a consequence. Besides, from Fig. 12, the quality factor Q increases dramatically when the conduction angle decreases. Thus, a small conduction angle is not desirable in the HV generator. In this paper, $\theta = 2/3\pi$ is empirically selected by experience to balance the voltage gain requirement and stresses of components.
3) Quality factor Q : Q is selected under the premise of (36). When $\theta = 2/3\pi, Q > 1.27$. From (35), a large Q value means a large series inductance. The power losses and the volume of inductor will increase as a result. Low Q value means poor frequency selectivity of the resonant tank, leading to large harmonic resonant currents. So, Q should be selected neither too large nor too small. Q is suggested in the range of 2.5–20 [32].

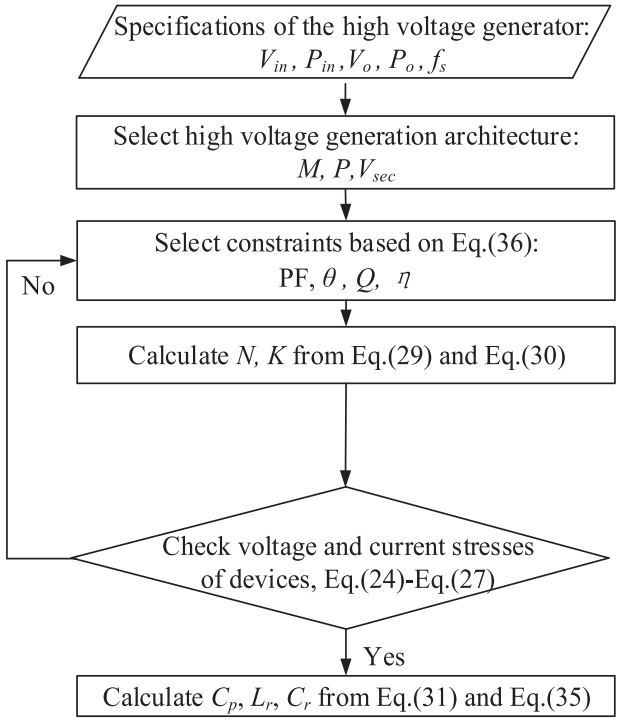

Fig. 13. Design flowchart of the HV generator.

Finally, after selection of Q, PF, and θ, the parameters to be designed include the turns ratio, the parallel capacitor, the resonant inductor and capacitor. They can be calculated by (31) and (33) directly. A design flowchart of HV generator is given in Fig. 13.

V. Experimental Results

A 500 W 20 kV HV generator with architecture 4 (HV generator architecture with distributed transformer and multiplier) is designed and built to validate the analysis and design method. The specifications of the HV generator are shown in Table IV. The parameters in the design are provided in Table V. Based on the proposed design procedure, the parameters of the HV generator are shown in Table VI.

Fig. 14 shows the prototype of the HV transformers and voltage multipliers. The HV transformer magnetic core, secondary

TABLE IV
SPECIFICATIONS OF HV GENERATOR

Specifications	Value
Input voltage V_{in}	250 V
Output voltage V_o	20 kV
Output power P_o	500 W
Switching frequency f_s	400 kHz

TABLE V
DESIGN CONSTRAINTS

Parameters	Value
HV transformer output voltage V_{sec}	1.25 kV
Conduction angle θ	$\frac{2\pi}{3}$
Power factor PF	0.88
Quality factor Q	4.0
Designed efficiency η	0.80

TABLE VI
PARAMETERS OF DESIGNED HV GENERATOR

M	N	P	K	C_P/nF	L_{r_tot}/μH	C_r/nF	C_o/nF
2	2	2	4:45	3.5	88.0	2.5	1.5

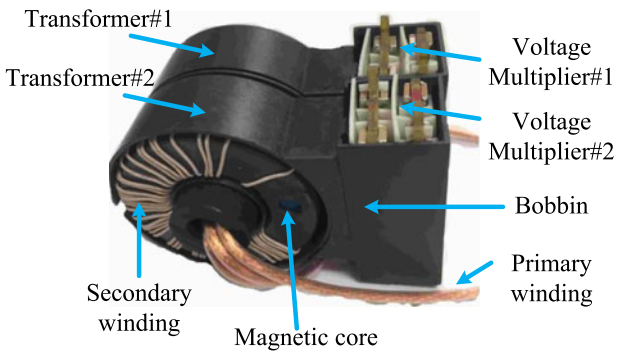

Fig. 14. Prototype of the HV transformer and the voltage multiplier.

winding and the voltage multiplier, are packaged in an integrated enclosure for the compact structure. The two HV transformers share the same primary winding.

The equivalent capacitance C_p is composed of the HV transformer secondary-side parasitic capacitance, the diode junction capacitance, and added parallel capacitance. In the HV transformer, the measured parallel capacitor is 7 pF. A SiC diode is chosen for high-frequency switching characteristics and the total diode junction capacitance is 5 pF, at 2.5 kV. Thus, another 2 nF parallel capacitor needs to be added to the primary side to satisfy the designed parallel capacitance. Besides, the measured total leakage inductance of the two HV transformers at the primary side is 2.0 μH; thus, the added series resonant inductance is 86.0 μH.

Fig. 15 illustrates the waveforms at full load and Fig. 16 illustrates the light-load condition at the same output voltage. The

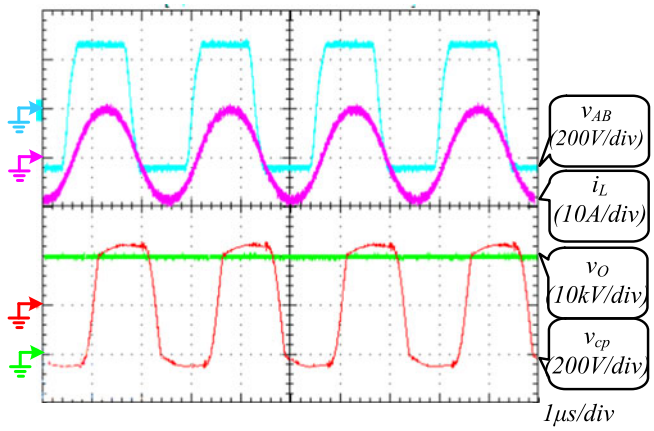

Fig. 15. Experiment waveforms at $P_o = 500$ W, $V_o = 20$ kV, and $f_s = 400$ kHz.

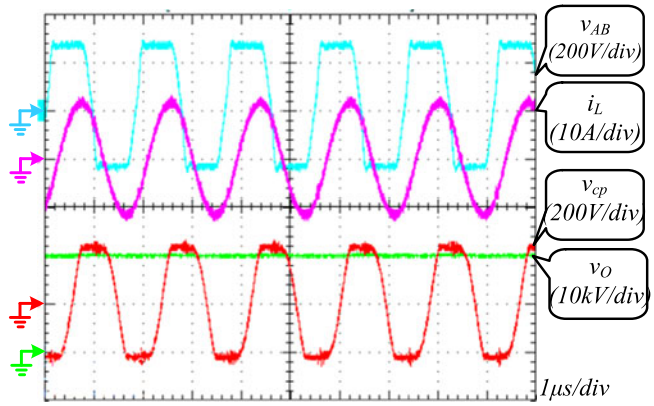

Fig. 16. Experiment waveforms at $P_o = 125$ W, $V_o = 20$ kV, and $f_s = 550$ kHz.

TABLE VII
COMPARISON BETWEEN THE EXPERIMENT AND MODEL

f_s/kHz	R_o/MΩ	V_o/kV			I_{Lm}/A		
		Experiment	Model	Error	Experiment	Model	Error
400	0.75	19.16	19.30	0.73%	4.80	4.86	1.27%
425	1.05	19.50	20.01	2.62%	3.91	3.84	–1.82%
450	1.35	19.69	20.18	2.49%	3.33	3.36	0.86%
465	1.50	19.55	20.17	3.17%	3.15	3.15	0.07%
482	1.80	20.09	21.10	5.03%	2.95	3.03	2.78%
504	2.10	19.28	20.91	8.45%	2.71	2.95	9.03%
520	2.40	20.14	22.39	11.17%	2.58	2.90	12.29%
539	2.70	19.68	22.99	16.82%	2.42	2.87	18.74%
550	3.00	19.83	23.30	17.50%	2.37	2.94	23.84%

waveform of inverter output voltage shows that the soft switching is fully realized under rated and light-load conditions. Under the light-load conditions, where the output power is 125 W, to maintain the same output voltage, the switching frequency rises to 550 kHz.

Table VII and Fig. 17 give a comparison between the model and the experiments. The results show a high degree of

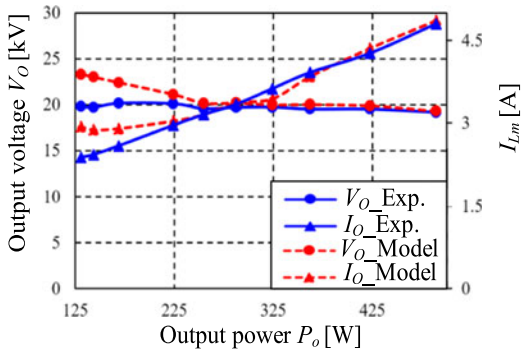

Fig. 17. Comparison between the experiments and proposed model.

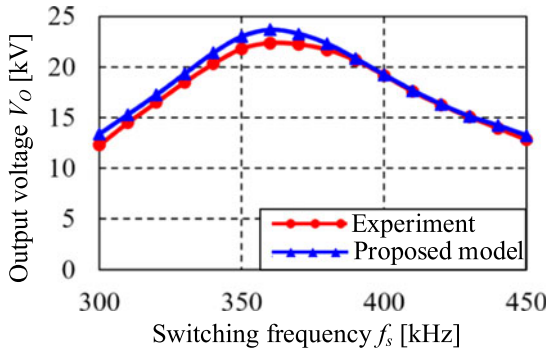

Fig. 18. Frequency response of the output voltage by experiment and proposed model.

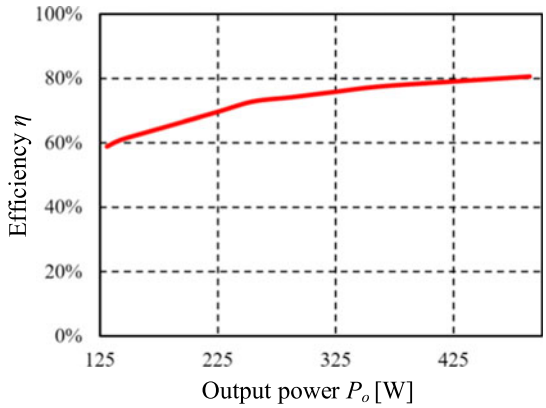

Fig. 19. Measured efficiency of the HV generator prototype.

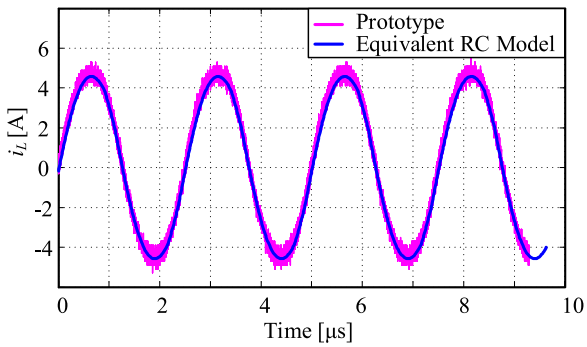

Fig. 20. Resonant current comparison between the experimental and the proposed model.

accuracy between the design and experiments in high output power areas, whereas under light-load conditions, the error between experiments and calculation is relatively large.

Fig. 18 gives the frequency response of the output voltage by the experiment and the proposed model. The model matches well with the prototype when the switching frequency is around 400 kHz, whereas a larger error occurs when the switching frequency is below or near the resonant frequency. The error between the model and the experiment mainly comes from the following aspects.

1) The designed efficiency $\eta = 0.8$ is not satisfied under light-load conditions or when the switching frequency is below or near the resonant frequency. From the efficiency diagram in Fig. 19, it can be seen that when the output power is around 500 W, the efficiency is around 0.8, and the analytical model gives results with acceptable error. However, when the output power decreases, the efficiency also decreases and the error increases. Similarly, when switching frequency is below or near the resonant frequency, the soft-switching conditions cannot be ensured. The circuit efficiency decreases, and hence the error increases.
2) The proposed model is derived under ideal conditions. Some nonideal factors are not included in the model, such as the voltage drop of diodes and the resistance of devices. These factors bring error between the model and prototype.

In Fig. 20, a comparison is made between the measured waveform and the equivalent circuit in Fig. 4. The purple line represents the experimental result of the resonant current. The blue line represents the calculated resonant current in which the HV generation circuit is replaced by the computed equivalent loading of $R_{\rm eq} = 99.1\,\Omega, C_{\rm tot} = 3.58$ nF. The two resonant currents match well, which verifies the validity of the proposed equivalent *RC* network of the HV generation architectures.

VI. Conclusion

A unified equivalent circuit model is proposed for various HV generator architectures with different voltage multiplier topologies, stage number, and polarities. These complicated HV structures can be decomposed into the basic circuit structure and then a generic equivalent circuit model is derived to simplify the converter analysis and design. Based on the equivalent circuit model of the HV generation circuit, power factor, voltage gain, and component stresses are analyzed and verified through simulation. Further, a general design method utilizing conduction angle, power factor, and quality factor achieves good performance in efficiency and component stresses. Finally, a high-frequency HV generator based on architecture 4 with two distributed HV transformers loaded by two-stage dual polarity CW voltage multipliers is designed and tested. The experimental results show high consistency with the proposed model around the designed operating points, which verifies the validity of the proposed model and comprehensive design methodology.

REFERENCES

[1] S. R. Jang, H. J. Ryoo, S. H. Ahn, J. Kim, and G. H. Rim, "Development and optimization of high-voltage power supply system for industrial magnetron," *IEEE Trans. Ind. Electron.*, vol. 59, no. 3, pp. 1453–1461, Mar. 2012.

[2] M. G. Giesselmann, T. T. Vollmer, and W. J. Carey, "100-kV high voltage power supply with bipolar voltage output and adaptive digital control," *IEEE Trans. Plasma Sci.*, vol. 42, no. 10, pp. 2913–2918, Oct. 2014.

[3] M. Jaritz, S. Blume, D. Leuenberger, and J. Biela, "Experimental validation of a series parallel resonant converter model for a solid state 115-kV long pulse modulator," *IEEE Trans. Plasma Sci.*, vol. 43, no. 10, pp. 3392–3398, Oct. 2015.

[4] S. Mao, C. Li, W. Li, J. Popovic, and J. Ferreira, "Review of high frequency high voltage generation architectures," in *Proc. IEEE 14th Int. Conf. Power Electron. ECCE Asia*, Jun. 2017, pp. 2260–2266.

[5] I. Batarseh, R. Liu, C. Q. Lee, and A. K. Upadhyay, "Theoretical and experimental studies of the LCC-type parallel resonant converter," *IEEE Trans. Power Electron.*, vol. 5, no. 2, pp. 140–150, Apr. 1990.

[6] R. Yang, H. Ding, Y. Xu, L. Yao, and Y. Xiang, "An analytical steady-state model of LCC type series–parallel resonant converter with capacitive output filter," *IEEE Trans. Power Electron.*, vol. 29, no. 1, pp. 328–338, Jan. 2014.

[7] J. A. Martin-Ramos, A. M. Pernia, J. Diaz, F. Nuno, and J. A. Martinez, "Power supply for a high-voltage application," *IEEE Trans. Power Electron.*, vol. 23, no. 4, pp. 1608–1619, Jul. 2008.

[8] J. A. Martin-Ramos, J. Diaz, A. M. Pernia, J. M. Lopera, and F. Nuno, "Dynamic and steady-state models for the PRC-LCC resonant topology with a capacitor as output filter," *IEEE Trans. Ind. Electron.*, vol. 54, no. 4, pp. 2262–2275, Aug. 2007.

[9] F. Cavalcante and J. W. Kolar, "Design of a 5 kW high output voltage series-parallel resonant DC–DC converter," in *Proc. IEEE Power Electron. Spec. Conf.*, 2003, pp. 1807–1814.

[10] T. B. Soeiro, J. Mühlethaler, J. Linnér, P. Ranstad, and J. W. Kolar, "Automated design of a high-power high-frequency LCC resonant converter for electrostatic precipitators," *IEEE Trans. Ind. Electron.*, vol. 60, no. 11, pp. 4805–4819, Nov. 2013.

[11] D. Fu, F. C. Lee, Y. Qiu, and F. Wang, "A novel high-power-density three-level LCC resonant converter with constant-power-factor-control for charging applications," *IEEE Trans. Power Electron.*, vol. 23, no. 5, pp. 2411–2420, Sep. 2008.

[12] J. S. Brugler, "Theoretical performance of voltage multiplier circuits," *IEEE J. Solid-State Circuits*, vol. 6, no. 3, pp. 132–135, Jun. 1971.

[13] W. C. Hsu, J. F. Chen, Y. P. Hsieh, and Y. M. Wu, "Design and steady-state analysis of parallel resonant DC-DC converter for high-voltage power generator," *IEEE Trans. Power Electron.*, vol. 32, no. 2, pp. 957–966, Feb. 2017.

[14] L. Katzir and D. Shmilovitz, "A matrix-like topology for high-voltage generation," *IEEE Trans. Plasma Sci.*, vol. 43, no. 10, pp. 3681–3687, Oct. 2015.

[15] L. Malesani and R. Piovan, "Theoretical performance of the capacitor-diode voltage multiplier fed by a current source," *IEEE Trans. Power Electron.*, vol. 8, no. 2, pp. 147–155, Apr. 1993.

[16] S. S. Lee, S. Iqbal, and M. Kamarol, "Control of ZCS-SR inverter-fed voltage multiplier-based high-voltage DC–DC converter by digitally tuning tank capacitance and slightly varying pulse frequency," *IEEE Trans. Power Electron.*, vol. 27, no. 3, pp. 1076–1083, Mar. 2012.

[17] S. Mao, "A high frequency high voltage power supply," in *Proc. Eur. Conf. Power Electron. Appl.*, Birmingham, U.K., 2011, pp. 1–5.

[18] M. Hu, N. Froehleke, W. Peters, and J. Boecker, "Multi-objective optimization of LCC resonant converter applied in VLF HV generator," in *Proc. 37th Annu. Conf. IEEE Ind. Electron.*, 2011, pp. 1456–1461.

[19] Z. Cao, M. Hu, N. Fröhleke, and J. Böcker, "Modeling and control design for a very low-frequency high-voltage test system," *IEEE Trans. Power Electron.*, vol. 25, no. 4, pp. 1068–1077, Apr. 2010.

[20] L. Katzir and D. Shmilovitz, "A split-source multisection high-voltage power supply for X-ray," *IEEE J. Emerg. Sel. Topics Power Electron.*, vol. 4, no. 2, pp. 373–381, Jun. 2016.

[21] A. J. Gilbert, C. M. Bingham, D. A. Stone, and M. P. Foster, "Normalized analysis and design of LCC resonant converters," *IEEE Trans. Power Electron.*, vol. 22, no. 6, pp. 2386–2402, Nov. 2007.

[22] N. Shafiei, M. Pahlevaninezhad, H. Farzanehfard, and S. R. Motahari, "Analysis and implementation of a fixed-frequency LCLC resonant converter with capacitive output filter," *IEEE Trans. Ind. Electron.*, vol. 58, no. 10, pp. 4773–4782, Oct. 2011.

[23] Y. A. Ang, C. M. Bingham, M. P. Foster, D. A. Stone, and D. Howe, "Design oriented analysis of fourth-order LCLC converters with capacitive output filter," *IET Power Electron.*, vol. 152, no. 2, pp. 310–322, 2005.

[24] N. Shafiei, M. Pahlevaninezhad, H. Farzanehfard, A. Bakhshai, and P. Jain, "Analysis of a fifth-order resonant converter for high-voltage DC power supplies," *IEEE Trans. Power Electron.*, vol. 28, no. 1, pp. 85–100, Jan. 2013.

[25] F. Cavalcante and J. W. Kolar, "Small-signal model of a 5 kW high output voltage capacitive-loaded series-parallel resonant DC-DC converter," in *Proc. Power Electron. Spec. Conf.*, 2005, pp. 1271–1277.

[26] L. Dalessandro, F. da Silveira Cavalcante, and J. W. Kolar, "Self-capacitance of high-voltage transformers," *IEEE Trans. Power Electron.*, vol. 22, no. 5, pp. 2081–2092, Sep. 2007.

[27] Y. Du, J. Wang, G. Wang, and A. Q. Huang, "Modeling of the high-frequency rectifier with 10-kV SiC JBS diodes in high-voltage series resonant type DC–DC converters," *IEEE Trans. Power Electron.*, vol. 29, no. 8, pp. 4288–4300, Aug. 2014.

[28] S. R. Sanders, J. M. Noworolski, X. Z. Liu, and G. C. Verghese, "Generalized averaging method for power conversion circuits," *IEEE Trans. Power Electron.*, vol. 6, no. 2, pp. 251–259, Apr. 1991.

[29] V. A. Caliskan, O. C. Verghese, and A. M. Stankovic, "Multifrequency averaging of DC/DC converters," *IEEE Trans. Power Electron.*, vol. 14, no. 1, pp. 124–133, Jan. 1999.

[30] J. A. Martin-Ramos, J. Diaz, A. M. Pernia, M. J. Prieto, and F. F. Linera, "Modelling of the PRC-LCC resonant topology with a capacitor as output filter using EDF," in *Proc. IEEE Power Electron. Spec. Conf.*, 2002, pp. 1337–1342.

[31] G. Ivensky, A. Kats, and S. Ben-Yaakov, "An RC load model of parallel and series-parallel resonant DC-DC converters with capacitive output filter," *IEEE Trans. Power Electron.*, vol. 14, no. 3, pp. 515–521, May 1999.

[32] A. J. Gilbert, "Analysis, design and control of LCC resonant power converters," Ph.D. dissertation, Dept. Electron. Elect. Eng., Univ. Sheffield, Sheffield, U.K., 2007.

[33] J. Wang, S. W. H. de Haan, and J. A. Ferreira, "Detailed derivation and minimization of the equivalent parasitic capacitances of a high-voltage multiplier based on the complete model," *IEEE Trans. Ind. Appl.*, vol. 51, no. 1, pp. 362–372, Feb. 2015.

Saijun Mao (M'15) was born in Jiangsu, China, in 1980. He received the B.Sc. and M.Sc. degrees in electrical engineering from Nanjing University of Aeronautics and Astronautics, Nanjing, China, in 2003 and 2006, respectively, and is currently working toward the Ph.D. degree in electrical engineering at Delft University of Technology, Delft, The Netherlands.

From 2006 to 2017, he was a Senior Engineer and Project Leader with GE Global Research Center, Shanghai, China. He has published more than 30 conference and journal papers. He holds more than 35 issued patents and pending patent applications. His research interests include wide-bandgap power semiconductor devices-based power conversion, high-frequency high-voltage generators, as well as harsh environment power conversion and packaging.

Dr. Mao was recipient of one IEEE Best Paper Award. He has been the recipient of more than 15 awards, including the Annual Technology Excellence Individual Award, Annual Technology Excellence Team Award, and Top Inventor Award in the GE Global Research Center.

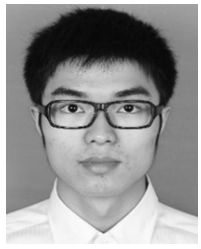

Chengmin Li received the B.Sc. degree in electrical engineering from the School of Electrical and Electronic Engineering, Huazhong University of Science and Technology, Wuhan, China, in 2013, where he is currently working toward the Ph.D. degree in electrical engineering.

From March 2015 to March 2016, he was a Research Intern with the GE Global Research Center, Shanghai, China. His research interests include applications of high-power converters and testing of high-power modules.

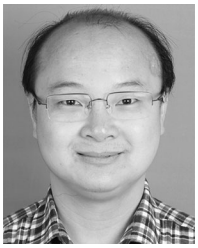

Wuhua Li (M'09) received the B.Sc. and Ph.D. degrees in power electronics and electrical engineering from Zhejiang University, Hangzhou, China, in 2002 and 2008, respectively.

From 2004 to 2005, he was a Research Intern, and from 2007 to 2008, a Research Assistant with the GE Global Research Center, Shanghai, China. From 2008 to 2010, he joined the College of Electrical Engineering, Zhejiang University, as a Postdoctoral Researcher. In 2010, he was promoted to Associate Professor. Since 2013, he has been a Full Professor with Zhejiang University. From 2010 to 2011, he was a Postdoctoral Fellow with the Department of Electrical and Computer Engineering, Ryerson University, Toronto, ON, Canada. He has published more than 200 peer-reviewed technical papers and holds more than 30 issued/pending patents. His research interests include power devices, converter topologies, and advanced controls for renewable energy-based power systems.

Dr. Li serves as an Associate Editor for the IEEE JOURNAL OF EMERGING AND SELECTED TOPICS IN POWER ELECTRONICS, *IET Power Electronics*, *CSEE Journal of Power and Energy Systems*, the Guest Editor of *IET Renewable Power Generation* for Special Issue "DC and HVDC system technologies," and a Member of the Editorial Board for *Journal of Modern Power System and Clean Energy*. He has been appointed as one of the Most Cited Chinese Researchers by Elsevier since 2014. Due to his excellent teaching and research contributions, he was recipient of the 2012 Delta Young Scholar Award from Delta Environmental and Educational Foundation, the 2012 Outstanding Young Scholar Award from the National Science Foundation of China, the 2013 Chief Scientist Award of the National Youth 973 Program, and the 2014 Young Top-Notch Scholar Award of the National Ten Thousand Talent Program. He was recipient of one National Natural Science Award and four Scientific and Technological Achievement Awards from the Zhejiang Provincial Government and the State Educational Ministry of China.

Jelena Popović (S'04–M'05) received the Dipl. Ing. degree in electrical engineering from the University of Belgrade, Belgrade, Serbia, in 2001, and the Ph.D. degree from Delft University of Technology, Delft, The Netherlands, in 2005.

From 2005 to 2011, she was with the European Center for Power Electronics (ECPE), as a Technology Transfer Coordinator for one of the ECPE flagship programs and working on various strategic activities related to power electronics-enabled energy efficiency. Since 2008, she has been with the Delft University of Technology as an Assistant Professor in power electronics, where she is currently a Guest Researcher from 2017. Her research interests include packaging and integration in power electronics, wide-bandgap power electronics, and off-grid rural electrification.

Stefan Schröder (S'98–M'03–SM'10) was born in Cologne, Germany. He received the Diploma and Doctoral degree from RWTH Aachen University, Aachen, Germany, in 1997 and 2003, respectively, both in electrical engineering.

In 1997, he became a Research Associate in the Institute for Power Electronics and Electrical Drives, RWTH Aachen University, where he worked on power electronic circuits and devices, particularly on high-power semiconductors. In July 2002, he became the Chief Engineer in the same institute and was responsible for research in the fields of electrical drives, power electronic circuits, and semiconductor devices. Since the beginning of 2005, he has been with GE Global Research Europe, Munich, Germany, now in the roles as a Senior Principal Engineer. He has been working on power electronic applications with a focus on high-power converters for medium-voltage drives, for renewable energy systems and grid-scale applications such as HVdc and Interties. He has authored or coauthored more than 60 published technical papers and filed 60 patents.

Dr. Schröder is a member of Verband der Elektrotechnik (VDE).

Jan Abraham Ferreira (M'88–SM'01–F'05) received the B.Sc., M.Sc., and Ph.D. degrees in electrical engineering from Rand Afrikaans University, Johannesburg, South Africa, in 1980, 1982, and 1988, respectively.

In 1981, he was with the Institute of Power Electronics and Electric Drives, Technical University of Aachen, and was a System Engineer at ESD Pty, Ltd., from 1982 to 1985. From 1986 to 1997, he was with the Department of Electrical Engineering, Rand Afrikaans University, where he held the Carl and Emily Fuchs Chair of power electronics in later years. Since 1998, he has been the Chair in power electronics and electrical machines with Delft University of Technology, Delft, The Netherlands, and served as the Head of the department during 2006–2010. He is the author and coauthor of 100 journal and transactions papers, 300 conference papers, and 15 patents.

Dr. Ferreira served as the President of the IEEE Power Electronics Society during 2015–2016. He was recipient of 15 Prize Paper Awards.